Differential toxicity of gold-doxorubicin in cancer cells *vs.* cardiomyocytes as measured by real-time growth assays and fluorescence lifetime imaging microscopy (FLIM)†

Eric Tawagi,[a] Charlotte Massmann,[a,b] Hicham Chibli[a] and Jay L. Nadeau*‡[a]

The kinetics of toxicity of doxorubicin (Dox) and gold nanoparticle-conjugated doxorubicin (Au-Dox) were investigated in cultured B16 melanoma cells and cardiomyocytes using real-time cell-growth imaging. Both bolus exposure and continuous exposure were used. Modeling of the growth curve dynamics suggested patterns of uptake and/or expulsion of the drug that were different for the different cell lines and exposures. Dox alone in B16 cells fit to a model of slow drug buildup, whereas Au-Dox fit to a pattern of initial high drug efficacy followed by a decrease. In cardiomyocytes, the best fit was to a model of increasing drug concentration which then began to decrease, consistent with breakdown of the doxorubicin in solution. Cardiomyocytes were more sensitive than B16 cells to Dox alone (IC_{50} 123 ± 2 nM *vs.* 270 ± 2 nM with continuous exposure), but were dramatically less sensitive to Au-Dox (IC_{50} 1 ± 0.1 µM *vs.* 58 ± 5 nM with continuous exposure). Bolus exposure for 40 min led to significant cell death in B16 cells but not in cardiomyocytes. Fluorescence lifetime imaging (FLIM) showed different patterns of uptake of Au-Dox in the two cell types that explained the differential toxicity. While Au-Dox concentrated in the nuclei of B16 cells, it remained endosomal in cardiomyocytes. These results suggest that stable conjugates of nanoparticles to doxorubicin may be useful for treating resistant cancers while sparing healthy tissue.

Introduction

Doxorubicin (Dox) is a cytostatic drug commonly used in the chemical treatment of a wide range of cancers. Its major drawback is a delayed cardiomyopathy which limits the cumulative dose given. Many pre-clinical and clinical studies have been conducted to try to reduce cardiotoxicity of Dox.[1] Current clinical trials focus mostly on administration of beta-blockers, anti-angiotensin agents, or iron chelators to high-risk patients receiving Dox.[2] Animal studies have investigated alternative approaches such as exercise,[3] dietary antioxidants,[4,5] lipid-lowering drugs,[6] and topoisomerase II inhibitors[7] to reduce cell damage caused by Dox.

Encapsulation or conjugation of Dox into/onto nanoparticles can also be cardioprotective because of altered pharmacokinetics and pharmacodynamics of the nanoparticle formulation. The enhanced permeability and retention (EPR) effect causes nanoparticles to selectively accumulate in tumor tissues, with less accumulation in healthy tissue, reducing exposure of non-target organs to Dox.[8,9] Clinical trials have confirmed significant decreases in cardiotoxicity with both PEGylated and non-PEGylated liposomal formulations of Dox.[10–12] An anthracycline, Dox has multiple modes of cytotoxic action, including intercalation into DNA.[13] However, it can also cause membrane damage; conjugation of Dox to large particles that do not enter the nucleus does not eliminate Dox toxicity[14] but changes its mechanism of action from pure apoptotic cell death to caspase-independent mechanisms. Because of these altered kinetics and mechanisms, conjugated Dox has been shown to be able to overcome cellular resistance in cancer cells that have high native resistance or treatment-induced resistance, such as melanoma cells.[15,16] Our previous research reported a stable conjugate of ultrasmall (2.7 nm) Au nanoparticles to Dox, where tiopronin-capped Au particles are

[a]Department of Biomedical Engineering, McGill University, 3775 University Street, Montreal, Quebec H3A 2B4, Canada. E-mail: jnadeau@caltech.edu

[b]Biomedical Technologies, Faculty of Medicine, University of Tübingen, Geissweg 5/1, 72076 Tübingen, Germany

†Electronic supplementary information (ESI) available: Schematic of conjugation reaction; images of cell detection using discrete object vs. field analysis; comparison of growth curves using discrete object vs. field analysis; dose–response curves obtained from real-time counts vs. endpoint colorimetric assays; growth curves of cardiomyocytes after bolus application of Dox and Au-Dox; lifetime fit values. See DOI: 10.1039/c5an00446b

‡Current address: GALCIT, California Institute of Technology, 1200 E. California Blvd, Pasadena, CA 91125. E-mail: jnadeau@caltech.edu

attached to Dox *via* an amide bond. Endpoint toxicity assays showed that Au-Dox was up to 20-fold more cytotoxic to resistant B16 murine melanoma cells than the equivalent concentration of Dox alone. However, Au-Dox was less cytotoxic to Dox-sensitive HeLa cells than was free Dox.[17]

There are several studies in the literature that examine the *in vitro* pharmacokinetics of Dox and liposomal Dox,[18–20] with modeling and extraction of model parameters from end-point cytotoxicity assays taken at different time points. One study compared free Dox and liposomal Dox in B16 cells, finding that liposomal Dox was significantly more effective at cell killing and that it entered cells more quickly. Nevertheless, the lag time between drug application and cell death was similar for free and encapsulated drug.[18] Another study modeled Dox uptake after continuous or time-limited exposure to free drug or drug encapsulated in protocells,[19] finding a similar result as with liposomes: the protocells entered the cells more quickly and led to more efficient cell death, particularly in resistant cell lines. The importance of exposure time of the drug and of drug uptake into subcellular compartments was emphasized in a third study.[20] Because of the multiple modes of action of Dox, the rates of entry vary; membrane binding, for example, occurs on a faster time scale than entry into nuclei or mitochondria. Dox-resistant cells show different rates of uptake of Dox into different cell compartments, as well as different threshold values.

In this study, we hypothesized that real-time imaging and growth analysis of cells exposed to Dox and Au-Dox would emphasize and help elucidate the different mechanisms of action of the two formulations. We tested this on a Dox-resistant, fast-growing melanoma cell line (B16) as well as a rat myocardial cell line with a slow division time and no resistance to Dox. The real-time cell growth method is based upon a multimode microplate platform coupled to an imaging cytometer. The instrument uses phase-contrast microscopy along with cell detection technology to analyze cell confluence without the use of cell labeling. Growth curves were complemented by fluorescence lifetime imaging (FLIM) analysis. FLIM is a concentration-independent imaging technique that is able to distinguish free from encapsulated Dox.[21–24] We previously used FLIM to observe uptake of Dox and Au-Dox into B16 cells, finding that Au-Dox was able to enter cell nuclei after approximately 4 h of incubation. The intact Au-Dox conjugate could be directly observed as a slow component to the lifetime.[25] These techniques clearly illustrate patterns of uptake and/or expulsion of free and conjugated doxorubicin that are different for the two cell lines. This has implications for designing Dox conjugates that are more effective against cancer cells and less toxic to the heart.

Experimental

Cell culture

Cell types used were B16 melanoma cells (a gift of J. Teodoro at the McGill Cancer Centre) and a myoblastic cell line (ATCC

CRL-1446) derived from embryonic BD1X rat heart tissue. The cells were cultured in high-glucose DMEM (Invitrogen Canada, Burlington, ON) supplemented with penicillin (100 U mL^{-1}), streptomycin (100 µg mL^{-1}), and FBS (10%), and incubated in a CO_2 humidified atmosphere. Cells were passaged at 5×10^3 cells per well (for B16) or at 4×10^3 cells per well (for cardiomyocytes) in 96 well culture plates 24 h before use. To obtain even distribution of the cells, the culture plate was gently rocked five times from left to right, and five times from far to near for a total of five times, and left in the biosafety cabinet for 40 min before placing into the incubator.

Synthesis of Au nanoparticles and Au-Dox

Ultrasmall particles capped with tiopronin were made by a published method[26] involving addition of hydrogen tetrachloroaureate(III) trihydrate and tiopronin (N-(2-mercaptopropionyl) glycine) to an aqueous solution of sodium borohydrate. After vigorous stirring for 30 min, the resulting black solution was collected, concentrated, dissolved in H_2O and dialyzed for 72 h against dH_2O (2 L), which was changed every 12 h. Particles were characterized by transmission electron microscopy (TEM), Fourier transform infrared spectroscopy (FTIR), and absorbance/emission spectroscopy. For conjugation to Dox, a solution of borate buffer (20 mM, pH 9) containing Au nanoparticles (1 µM), EDC (1 mM) and NHS (2 mM) was stirred for 1 h before adding the Dox to a final concentration of 25 µM. The mixture was stirred at 25 °C for 12 h. The conjugates were purified by ultrafiltration (Vivaspin 5000 KDa filters) and resuspended in phosphate-buffered saline (PBS), pH 7.4. The amount of Dox per Au nanoparticle was calculated based upon the absorbance of Dox at 500 nm in the purified conjugates, as reported previously.[17]

Toxicity studies

The IC$_{50}$ of Dox and Au-Dox were determined using the SRB assay and real-time growth curve imaging sequentially on the same plates. When the cells were 60% confluent, the media was removed and the cells were incubated with Dox alone or Au-Dox at various concentrations in supplemented DMEM. After 30 min, they were washed with PBS and incubated in 200 µL of supplemented DMEM. Next, the cells were imaged on a SpectraMax® MiniMax 300 Imaging Cytometer (Molecular Devices) with the transmitted light channel at different time points. Measurements took approximately 7 minutes and cells were returned to the incubator between measurements. Immediately after the last time point measurement, the cells were fixed with trichloroacetic acid (65 µL of 40% v/v) at 4 °C overnight, then washed five times with distilled water, air-dried for at least 40 min, and stained with SRB reagent (sulforhodamine B) (50 µL) for 30 min. Unbound SRB was removed by washing four times with 1% acetic acid and the plate was air-dried for at least 40 min; bound SRB was dissolved in Tris (100 µL of 10 mM solution at pH 10.5). Absorbance was read at 510 nm using a SpectraMax® i3 microplate reader from Molecular Devices.

Cell imaging

Cells were imaged at 37 °C with the SpectraMax® MiniMax 300 Imaging Cytometer with predefined settings. Imaging was done using the transmitted light channel and nine images per well were taken. The confluence of the cells was then measured with a custom user-defined field analysis setting on the SoftMax Pro software (Molecular Devices). The region of interest for each well delineated the middle ninth area. Four to six cells with normal morphology, bright and differentiated, were delineated as positive hits, while four to six dead cells, darkened and rounded in addition to regions without cells were delineated as negative hits. From our selections, the analysis was defined by the software and the effectiveness of the analysis was assessed qualitatively.

In order to determine the best approach to imaging-based cytotoxicity, we tested two modes of cell analysis: object analysis and field analysis. Object analysis measures the cell counts and is reported as the number of cells per well (cell count). Field analysis measures cell confluence and is reported as percentage of the well area covered by cells (% area covered). The methods were optimized on both B16 cells and cardiomyocytes by training the software with cell shapes of live (countable) and dead (undesirable) cells in addition to color of dead cells using a trial and error approach until the best cell demarcation was reached. The selection and optimization process was reiterated at least five times or until the analysis led to a majority of live cells being chosen by the software at different cell confluences.

Data analysis and curve fitting

Real-time growth curve data were analyzed using Mathematica 10 (Wolfram). Quality of fits was determined by sum of squared errors (SSE); the number of free parameters was minimized by checking the goodness of fit after eliminating each parameter. The SRB data were evaluated using GraphPad Prism and were fit to the Hill equation.

FLIM

Cells on glass-bottom dishes were incubated with Au-Dox at 1 μM of Dox (40 nM of Au) for 1 h or 4 h in Extreme DMEM (Wisent, Quebec, Canada). After incubation, cells were washed twice with PBS, fixed with 2% of paraformaldehyde at 4 °C for 10 min, and washed 3 times with ice-cold PBS before imaging in PBS. Fluorescence lifetime images were acquired on a Zeiss LSM710 SPAD microscope outfitted with a PicoQuant LSM FLIM upgrade kit consisting of a FLIM excitation source, internal laser bypass, and single-photon avalanche diode (SPAD) detector. The excitation source was a 473 nm pulsed laser operated at a 50 MHz pulse rate (time resolution, 400 ps). Parameters were chosen so that unlabeled cell autofluorescence did not yield a measurable signal (zero counts). Signals were collected with a 590 nm long-pass filter for 90s with the pinhole open at 441.2 nm, and the gain set to 800. Data were analysed using SymPhoTme 64 (PicoQuant). Lifetime decays were fit to a dual exponential decay model of the form:

$$I/I_0 = A_1 e^{-t/\tau_1} + A_2 e^{-t/\tau_2} \tag{1}$$

where A are the amplitudes and τ are the fluorescence lifetimes. The instrument response function (IRF) was deconvolved from the signal. Goodness-of-fit data and residuals were used to gauge fit results; a χ^2 between 0.9–1.1 and random distribution of residuals around the x-axis were necessary for a fit to be considered accurate.

Results and discussion

Particle synthesis and characterization

Au nanoparticle size can be controlled by the concentration of reductants in the reaction. We chose to produce particles of ~3 nm as our previous results had found that particles of this size were able to enter cell nuclei, and that Au-Dox conjugates using these particles were effective against B16 melanoma *in vitro*[17] and *in vivo*.[27] As produced, the Au-tiopronin nanoparticles were uniform in size, with a diameter of 2.7 ± 0.8 nm as measured by transmission electron microscopy (Fig. 1). Approximately 25 Dox molecules were attached per particle by an amide bond between the carboxylate of the tiopronin and the primary amine of Dox (ESI Fig. S1† for a schematic). This is a stable bond that does not release measurable free Dox after 24 h4 at pH 5 or ph 7.[25]

Image acquisition for real-time cell proliferation curves

Field analysis proved to be more reliable than object analysis for the cell proliferation measurements, as object analysis failed to detect all the desired cells (See ESI Fig. S2†). This was therefore the method used for all of the cytotoxicity experiments. The wells on the perimeter of the plate (outermost wells) were plated with cells for comparison but were not analyzed because of edge effects. More rapid evaporation in those wells caused cells to aggregate towards the outer edges, resulting in non-uniform cell coating. Similarly, when choosing the area to analyze, it was preferable to choose the centers of the wells because of non-uniform growth and difficulties with
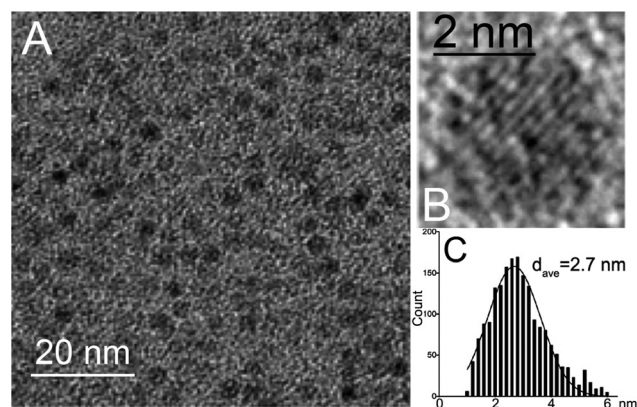
Fig. 1 Characterization of Au nanoparticles and conjugates. (A) TEM image of Au nanoparticles. (B) High-resolution TEM showing crystal structure of a single particle. (C) Histogram of particle sizes for >2000 particles.
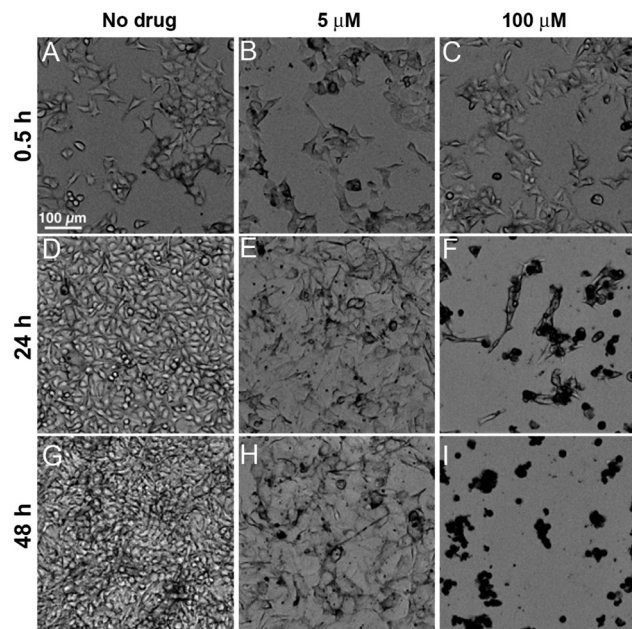
Fig. 2 Phase-contrast images of B16 cells after (A–C) 0.5, (D–F) 24, and (G–I) 48 h of exposure to doxorubicin at 0 μM, 5 μM, and 100 μM.

Fig. 3 Phase-contrast images of B16 cells after (A–C) 0.5, (D–F) 24, and (G–I) 48 h of exposure to Au-Dox at (1) 0 μM, (2) 0.6 μM and (3) 50 μM. Note the shrunken appearance of the cells in Panel F as compared with the same panel in Fig. 2. Slight focusing differences along with differences in melanin expression account for the difference in appearance of the untreated cells.

imaging at the edges of the wells. Both imaging methods yielded B16 doubling times of 12 ± 1 h, consistent with literature results (see ESI Fig. S3†).

As expected, the cells' features were affected by the drugs. In Dox-treated cells, morphological changes commonly observed in apoptotic cells were apparent (shrinkage, rounding, detachment)[28] in addition to significant darkening of the cells[29] (Fig. 2). Au-Dox appeared similar, but with more cell shrinkage associated with caspase-independent cell death, and with comparable amounts of cell death occurring at lower concentrations than with Dox alone (Fig. 3).

Real-time growth curves illustrate different kinetics of Dox and Au-Dox

B16 cells with short drug exposure (washed). Real-time curves of cell confluence as measured by the field analysis method are shown in Fig. 4 for B16 cells exposed to doxorubicin or Au-Dox for 40 minutes, then washed (time 0 is measured from when the drug was added). In the absence of drug. growth is described by the logistic equation

$$\frac{dN}{dt} = cN\left(1 - \frac{N}{N_{max}}\right), \qquad (2)$$

where N is the number of cells, k is a growth rate, and N_{max} is the maximum number of cells in the well (or, for field analysis, the maximum confluence as measured by the value at plateau in the absence of drug). The solution to this is a Boltzmann sigmoid[30]

$$N(t) = \frac{N_{max}}{1 + \left(\frac{N_{max} - N_0}{N_0}\right)e^{-ct}} \equiv \frac{N_{max}}{1 + e^{(N_{50} - k)t}} \qquad (3)$$
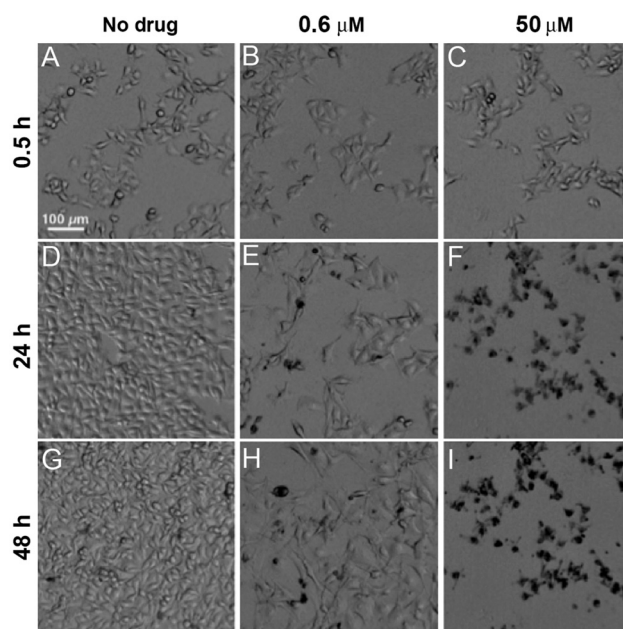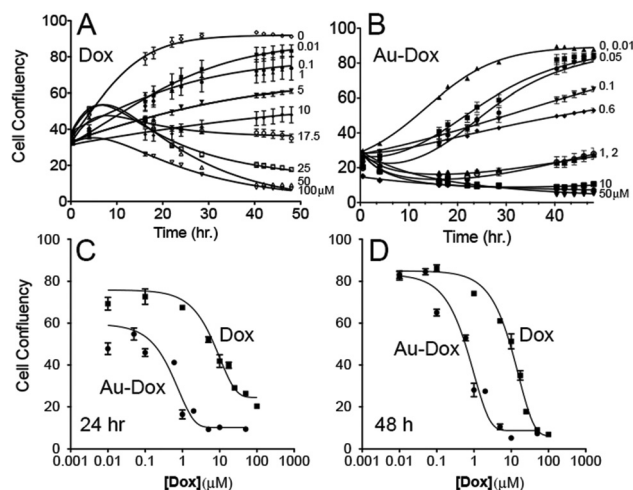

Fig. 4 Growth curves and dose–response for B16 cells exposed to drug for 40 minutes, then washed. (A) Real-time plot of B16 cell confluence after incubation with Doxorubicin at 0, 0.01, 0.1, 1, 5, 10, 17.5, 25, 50, and 100 μM and (B) Real-time plot of B16 cell confluence after incubation with Au-Dox at 0, 0.01, 0.05, 0.1, 0.6, 1.0, 2.0, 10, and 50 μM. The data points are measurements, and the curves are fits to eqn (6) or (7) with parameters given in Table 1. Each data point is the mean of six replicates with error bars indicating standard error of the mean (SEM). (C) Dose–response at 24 h. The curve for Dox had not plateaued and thus did not yield a reliable IC$_{50}$ value. (D) Curves at 48 h showing maximal effect for both drugs. (See Table 3 for fit values).

where N_0 is the number of cells at time $t = 0$, and N_{50} is defined as the half-maximum point of the curve. With the addition of drug, a death term b is introduced into eqn (1), giving

$$\frac{dN}{dt} = -bN + cN\left(1 - \frac{N}{N_{max}}\right). \tag{4}$$

This equation may also be solved analytically to yield a similar sigmoid form that is a function of $c - b$:

$$N(t) = \frac{(c-b)N_{max}}{c - e^{-(c-b)t}e^{-[i\pi + \log N_0 - \log((c-b)N_{max} - cN_0)]}} \tag{5}$$

However, this is only applicable when the drug concentration is constant at its site of action. Given the slow uptake rate of Dox, it was necessary to take into account a time delay for accumulation. This may be modeled as a concentration that plateaus after a characteristic time a[31,32]:

$$\frac{dN}{dt} = -b(1 - e^{-t/a})N + cN\left(1 - \frac{N}{N_{max}}\right) \tag{6}$$

The plateau phase decreased in duration with increasing drug concentration, lasting ~20 h at 10 μM and only ~10 h at 100 μM (Fig. 4A, Table 1). The values of a correspond to the physically measurable duration of the plateau before cell death. The absolute values of b and c do not have physical meaning, but their ratio gives a measure of cell killing *vs.* cell growth; c/b was almost a monotonically decreasing function of

Table 1 Fits to eqn (6) (for Dox alone washed) or eqn (7) (for Dox alone unwashed and Au-Dox both washed and unwashed) according to drug and concentration

	a	b	c	c/b
B16 Control	0	0	0.15	—
B16Dox alone 0.01 μM	2.90	0.011	0.075	6.82
B16Dox alone 0.1 μM	0.109	0.0027	0.075	27.8
B16Dox alone 1 μM	2.99	0.024	0.118	4.92
B16Dox alone 5 μM	1.93	0.017	0.064	3.76
B16Dox alone 10 μM	1.00	0.019	0.05	2.63
B16Dox alone 17.5 μM	5.05	0.132	0.216	1.64
B16Dox alone 25 μM	10.2	0.198	0.221	1.12
B16Dox alone 50 μM	20.4	0.272	0.195	0.717
B16Dox alone 100 μM	10.3	0.111	0.067	0.604
Dox 0.01 μM unwashed	0.995	0.078	0.094	1.21
Dox 0.1 μM unwashed	0.047	0.079	0.116	1.47
Dox 0.3 μM unwashed	0.461	0.189	0.044	0.233
Dox 1 μM unwashed	0.732	0.129	0.020	0.155
Dox 6 μM unwashed	0	0.003	0	0
B16AuDox 0.01 μM	0.050	0.263	0.259	0.98
B16AuDox 0.05 μM	0.050	0.170	0.210	1.24
B16AuDox 0.1 μM	0.050	0.011	0.043	3.91
B16AuDox 0.6 μM	0.011	0.342	0.482	1.41
B16AuDox 1 μM	0.008	0.489	0.500	1.02
B16AuDox 2 μM	0.006	0.453	0.500	1.10
B16AuDox 5 μM	0.002	0.487	0.500	1.03
B16AuDox 10 μM	0	0.171	0.154	0.901
B16AuDox 50 μM	0	0.044	0	0
AuDox 0.01 μM unwashed	0	0.013	0.157	12.1
AuDox 0.05 μM unwashed	0	0.007	0.116	16.6
AuDox 0.1 μM unwashed	0	0.037	0	0
AuDox 0.6 μM unwashed	0	0.071	0	0

concentration for free Dox, with the exception being a spike at the lowest concentrations (Table 1).

The different kinetics of Au-Dox were apparent from the growth curves. Au-Dox was cytotoxic at lower effective Dox concentrations, and without a delay. The curves resembled sigmoids, but with an initial drop in cell confluence followed by a sigmoidal rise. The best fit was to an equation where concentration of the drug began at its highest level and then decreased:

$$\frac{dN}{dt} = -b(e^{-at})N + cN\left(1 - \frac{N}{N_{max}}\right) \tag{7}$$

There was some recovery of cells in the Au-Dox case after ~40 h. This was not seen with Dox alone (Fig. 4B). The values of c/b were markedly smaller than for free Dox even for low concentrations of Au-Dox (Table 1), suggesting that cell killing dominated cell growth even for low concentrations. The spike at low concentrations was also seen here; sub-toxic concentrations of Dox have been shown to stimulate cell growth, especially if the medium is sub-optimal,[33] consistent with our measurements.
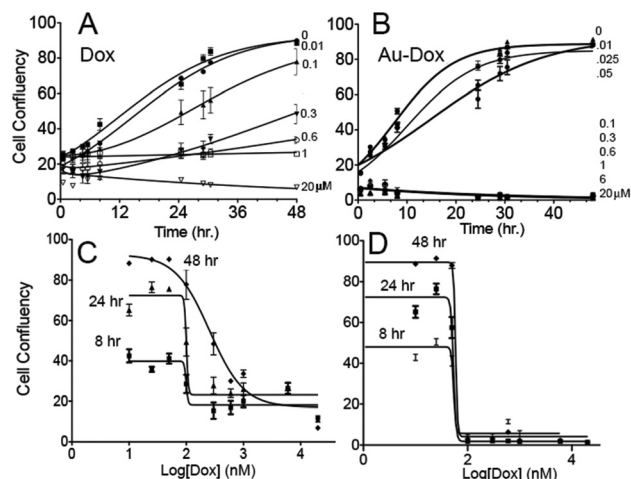
A half inhibition constant (IC_{50}) of a drug could be estimated at any time point from the real-time growth curves by taking a slice through the data curve at the selected time point to yield a concentration-dependent curve. Fig. 4C shows the results at 24 h, which illustrated that Dox alone had not yet had its full effect. Even at the highest concentrations, many cells remained. Because the curve did not reach a lower limit, an IC_{50} value could not reliably be determined. On the other hand, Au-Dox had already achieved maximal effects at concentrations ≥1 μM. Fig. 4D shows the results at 48 h, where IC_{50} values could be determined for both Dox (16 μM) and Au-Dox (610 nM). This indicates more than a 20-fold increase in the cytotoxicity of Au-conjugated Dox relative to Dox alone in the case of short exposure followed by washing, in good agreement with previous work.[17] The values obtained from the real-time growth curves at 48 h were compared with results from the SRB endpoint assay and found to agree within 10% (see ESI, Fig. S4†).

B16 cells with continuous exposure (unwashed). When Dox was not removed from the cells during incubation, the initial plateau before cytotoxicity was not seen. Both Dox and Au-Dox curves fit best to eqn (7), although in the case of Au-Dox, concentrations above 100 nM led to simple exponential decay of cells (Fig. 4A and B). The IC_{50} of Dox alone was reduced 60-fold, to 270 nM (Fig. 5C). For Au-Dox, the IC_{50} was reduced 8-fold, to 58 nM, with full effects apparent as early as 8 h post exposure (Fig. 5D).

Cardiomyocytes. Because of the slow doubling time of the cardiomyocytes, measurements were carried out for 72 h after drug addition. Washing of cells after 40 min did not lead to significant cell death even at 5 μM (see ESI Fig. S5†). This was probably due to the shortness of the exposure time relative to the cell cycle time.[34] When drug was applied without washing, neither eqn (6) nor (7) yielded a good fit to the data. An

Fig. 5 Growth curves and dose–response for B16 cells exposed to drug continuously without washing. (A) Real-time plot of B16 cell confluence after incubation with Doxorubicin at 0, 0.01, 0.1, 0.3, 0.6, 1, and 20 μM. (B) Real-time plot of B16 cell confluence after incubation with Au-Dox at 0, 0.01, 0.025, 0.05, 0.1, 0.3, 0.6, 1, 6, and 20 μM. The data points are measurements, and the curves are fits to eqn (7) with parameters given in Table 1. Each data point is the mean of six replicates with error bars indicating standard error of the mean (SEM). (C) Dose–response for Dox alone at 8, 24, and 48 h. (D) Dose–response for Au-Dox at 8, 24, and 48 h (see Table 3 for fit values).
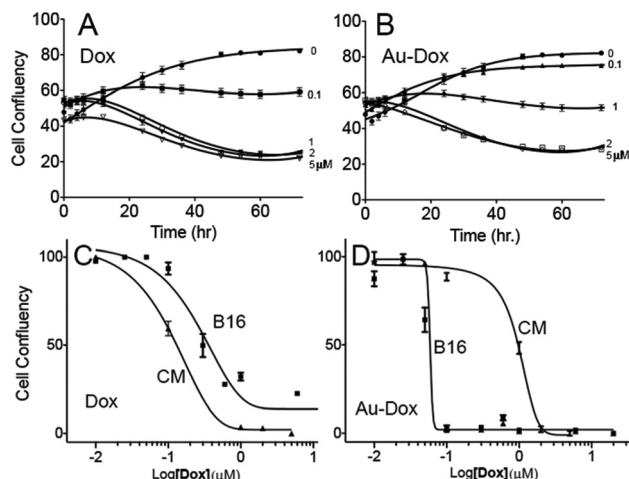
Fig. 6 Growth curves and dose–response for cardiomyocytes exposed to drug continuously without washing. (A) Real-time plot of cell confluence after incubation with Doxorubicin at 0, 0.1, 1, 2, 5 μM. (B) Real-time plot of cell confluence after incubation with Au-Dox at 0, 0.1, 1, 2, and 5 μM. The data points are measurements, and the curves are fits to eqn (8) with parameters given in Table 2. Each data point is the mean of six replicates with error bars indicating standard error of the mean (SEM). (C) Dose–response for Dox alone at 48 h comparing B16 cells and cardiomyocytes (CM). (D) Dose–response for Au-Dox at 48 h comparing B16 cells and cardiomyocytes (CM).

equation with 4 parameters, modeling the drug concentration as a parabola, was able to fit both the early plateau phase and the late recovery seen in these cells:

$$\frac{dN}{dt} = -b(at + dt^2)N + cN\left(1 - \frac{N}{N_{max}}\right) \quad (8)$$

Fig. 6A, B and Table 2 give the results of fits to eqn (8). Fig. 6C and D shows dose–response at 48 h, showing that cardiomyocytes were somewhat more sensitive than B16 cells to Dox alone (IC_{50} of ~120 vs. 270 nM), but much less sensitive to Au-Dox (IC_{50} of 1 μM vs. 58 nM).

The parameters a and d should not be considered to have much physical meaning on their own, but plots of the effective drug concentration parabolas defined by the parameters illustrate the different kinetics of Dox and Au-Dox. The effective concentration of Dox alone climbed rapidly and then rapidly decayed. However, the effective concentration of Au-Dox fell much more slowly; these curves could be approximated by eqn (5), whereas the Dox-alone values were very poorly fit to eqn (5) (Fig. 7). These results are consistent with previous studies investigating the stability of Dox in aqueous solution. Dox is most stable at acidic pH (pH 4) and 4 °C, but degrades at physiological pH and temperature, with a half-life of 50 h at 37 °C in phosphate buffer.[35] This matches very well the time course of the cardiomyocyte experiments; the experiments with B16 cells did not go on long enough for degradation to play a significant role. Conjugation to the gold appears to have delayed the ordinary breakdown process of the drug.

Table 2 Fits to eqn (8) for Dox alone Au-Dox unwashed applied to cardiomyocytes (CM)

	a	b	c	c/b	d
CM control	0	0	0.057	—	0
CM Dox alone 100 nM	0.487	1.58×10^{-3}	0.051	0.057	-5.31×10^{-3}
CM Dox alone 1 μM	0.174	0.012	0.028	0.051	-2.40×10^{-3}
CM Dox alone 2 μM	0.230	9.53×10^{-3}	0.035	0.028	-2.92×10^{-3}
CM Dox alone 5 μM	0.209	9.80×10^{-3}	0.027	0.035	-2.80×10^{-3}
CM AuDox 100 nM	0.151	1.31×10^{-3}	0.055	0.027	-1.31×10^{-3}
CM AuDox 1 μM	0.223	3.61×10^{-3}	0.040	0.055	-2.30×10^{-3}
CM AuDox 2 μM	0.088	0.018	0.010	0.040	-1.37×10^{-3}
CM AuDox 5 μM	0.166	3.13×10^{-3}	−0.020	<0	-3.91×10^{-3}

Table 3 IC_{50} values for the different experimental conditions determined at the 48 h time point. CM, cardiomyocytes. The values for washed CM were not determined. The errors represent standard errors from the curve fit

Condition	IC_{50} at 48 h Dox	IC_{50} at 48 h Au-Dox
B16 washed	16 ± 1 μM	610 ± 2 nM
B16 unwashed	270 ± 2 nM	58 ± 5 nM
CM unwashed	123 ± 2 nM	1.0 ± 0.1 μM

FLIM. In our previous work,[36] we characterized the lifetimes of Dox and Au-Dox in solution and in B16 cells using FLIM. Free Dox shows a longer lifetime in cell cytoplasm (~2.5 ns) than in nucleus (~1.2 ns); an additional small reduction in lifetime has been reported when free Dox intercalates DNA,
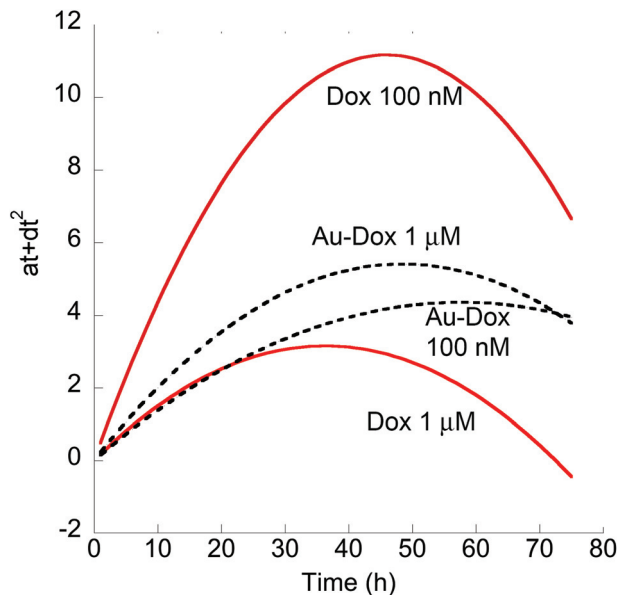
Fig. 7 Parabolic fits to effective drug concentrations (eqn (8)) for Dox and Au-Dox at two concentrations. Note the steeper slope of decline for Dox alone.

but this is difficult to resolve in cells. In solution, Au-Dox does not show a significant difference in lifetime compared to Dox alone, but in cells it is visible as a long-lifetime component (~4 ns). This component may be replicated *in situ* by adding lipids or membranes to Au-Dox, indicating that the long life-

time component results from membrane association. Au-Dox lifetimes do not change with DNA addition, so it is not possible to determine whether Au-Dox intercalates DNA using FLIM.

In the current study, we observed intact Au-Dox using FLIM by monitoring the long-lifetime component. In B16 cells, this long component appeared after 4 hours of incubation, showing that Au-Dox entered the nucleus somewhat more slowly than the rest of the cell (Fig. 8A and B). Intensity images showed the highest fluorescence intensity in the nucleus and nuclear membrane of B16 cells (Fig. 8C). However, when performing these experiments with cardiomyocytes, we observed a different pattern. After 4 h, the lifetime in the nucleus was equivalent to that of Dox alone, with no slow component (Fig. 8D and E). Intensities were greatest in the perinuclear region, corresponding to endosomes/lysosomes (Fig. 8F). Two-exponential fits to lifetimes in the different compartments showed comparable values between B16 and cardiomyocytes in the cytoplasm at 1 and 4 h and in the nucleus at 1 h, but a striking difference in the slow component in the nucleus at 4 h (Fig. 9, Table S1†).

Differences between B16 cells and cardiomyocytes. Taken together, the growth curves and imaging results help explain the observed differences in IC_{50} observed in the two cell lines. Dox is a cell-cycle-dependent drug that is most effective against cells in the S and G2/M phase, and causes cell-cycle arrest in G2/M followed by apoptosis.[37] The growth curves for cardiomyocytes (Fig. 5) show similar patterns for Dox and Au-Dox, with growth inhibition at 0.1 μM free Dox or 1 μM
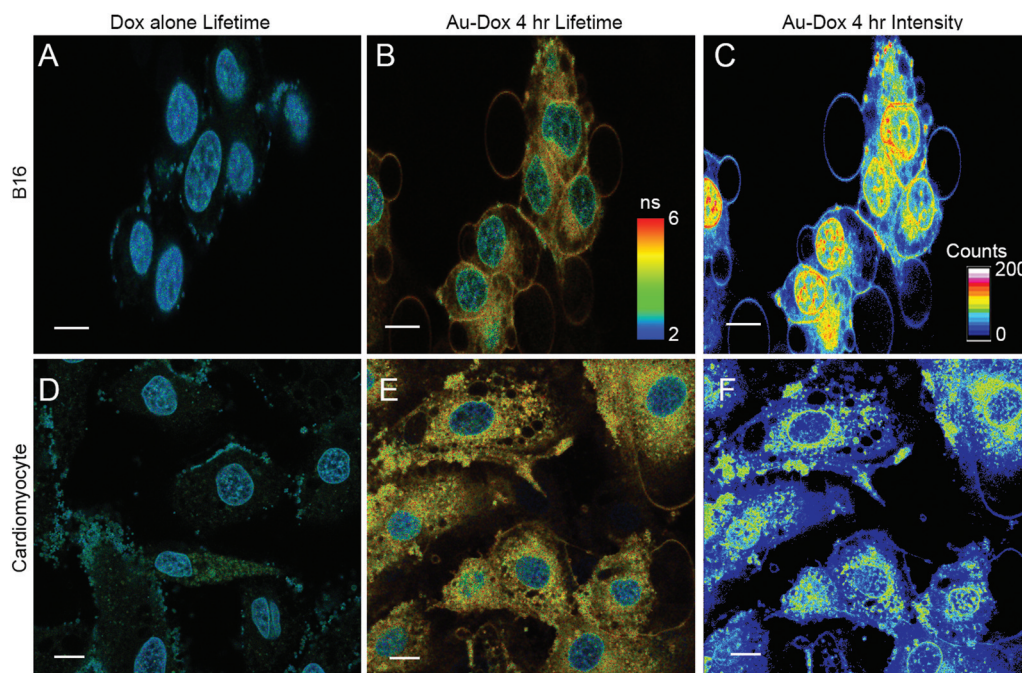

Fig. 8 FLIM images of B16 cells and cardiomyocytes exposed to Dox and Au-Dox. Scale bars are 10 μm; color-coded lifetime scale represents average lifetime and applies to all panels. (A) B16 with free Dox after 4 h. (B) B16 with Au-Dox after 4 h. (C) Intensity image of B16 with Au-Dox after 4 h. (D) Cardiomyocytes with free Dox after 4 h. (E) Cardiomyocytes with Au-Dox after 4 h. (F) Intensity image of cardiomyocytes with Au-Dox after 4 h.
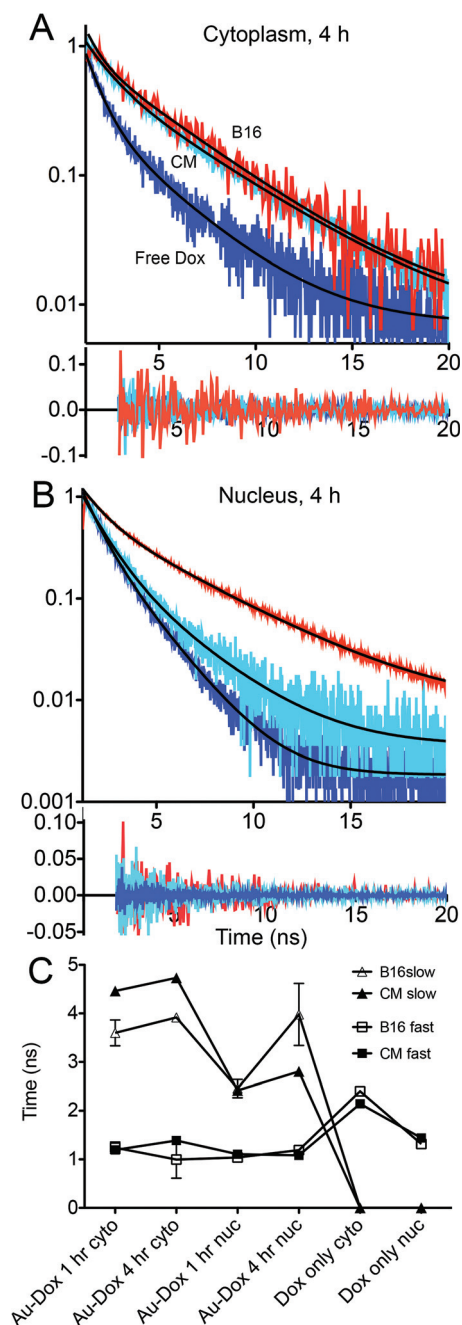
Fig. 9 Lifetime decay curves and fits. The solid black lines show fits with residuals given underneath the plots. (A) Cytoplasm after 4 h of incubation showing Au-Dox in B16 cells (red curve) and in CM (light blue). The free Dox curves for the 2 cell types overlapped, so only one curve is shown ("free Dox," dark blue). (B) Nucleus after 4 h of incubation showing Au-Dox in B16 cells (red) and CM (light blue). The free Dox curves for the 2 cell types overlapped so only one curve is shown ("free Dox," dark blue). (C) Fit values for dual-exponential fits to the fast and slow lifetime components in cytoplasm (cyto) and nucleus (nuc) after 1 and 4 h of incubation. The fast components (including the single component for free Dox) were equivalent in the two cell types. The slow component showed a dramatic difference between CM and B16 cells at 4 h, which was not seen at 1 h. The values are means of 7–10 regions or cells with error bars indicating standard deviation; when error bars do not appear, they are smaller than the symbols. The lines are guides for the eye. The values are given in the ESI, Table S1.†

Au-Dox. Combined with the imaging results, these curves suggest that Au-Dox is working in a similar fashion in these cells as free Dox. The conjugate is taken up into endosomes, and some free Dox is liberated by endosomal enzymes, where it is then able to enter the nucleus; effective concentrations with Au-Dox are lower than for free Dox since activity depends upon release. Future experiments will examine cell-cycle-synchronized cultures to determine the exact effects of cell cycle on toxicity, and will examine the effects of washing cells after incubation periods longer than 40 minutes.

In contrast to the cardiomyocytes, the mechanisms of action of Au-Dox *vs.* free Dox are different in B16 cells (Fig. 3 and 4). Free Dox delivered as a 40-min bolus shows a significant lag time before becoming effective, whereas Au-Dox is effective immediately. When the drug is not removed, Au-Dox leads to complete cell death at very low concentrations (100 nM and higher). A large number of studies have shown increased effectiveness of nanoparticle formulations of Dox in resistant cancer cells.[38] However, these formulations are all different from the one presented here, as nearly all of them focus upon drug release as a goal, with the nanoparticle being a delivery vehicle; none of them show intact entry of the conjugate into the nucleus. Examples of such constructs are Au-Dox made with a cleavable hydrazone bond,[39] and carbon nanotubes (CNTs) with Dox adsorbed by pi-stacking.[40] When the particles enter the cells, Dox is realeased and the free Dox enters the nucleus. These constructs are more effective against cancer cells than free Dox because of a reduced ability of the efflux pumps to expel the nanoparticle-bound Dox. Some other nanoparticle types release a modified form of Dox near the membrane that is not recognized by P-glycoprotein, the main moderator of resistance.[38] Some stable constructs have also been reported, such as Dox-transferrin, which do not release any Dox into the nucleus but which appear to kill cells through other mechanisms, such as membrane damage. Dox-transferrin is more effective against cancer cells than normal cells because of the overexpression of transferrin receptors by cancer cells, which results in greater nanoparticle uptake.[14,16]

Our conjugate is stable to hydrolysis and is found in the nuclei of B16 cells much more rapidly than can be explained by entry during mitosis. Thus, it appears that the construct either diffuses through the nucleopores or damages the nuclear membrane to an extent that permits entry. The FLIM and fluorescence intensity images do show enhancement of both the nuclear and nucleolar membranes, suggesting that Au-Dox associates primarily with membranes, though due to the small size it is certainly possible for it to pass through nucleopores, where the limit is ~6 nm.[41] The exact mechanisms of why this occurs to a great extent in B16 cells, and little or not at all in cardiomyocytes, remain to be explored. The kinetics of binding and entry of these ultrasmall particles also remains to be quantified, as the small size makes tracking individual particles difficult even by electron microscopy.

Numerous studies have shown that Dox resistance in cancer cells is primarily due to resistance to apoptosis.[42] Our first

study using ultrasmall Au-Dox showed that transfecting Dox-sensitive cells with the anti-apoptotic protein Bcl-2 protected them against Dox but not against Au-Dox.[17] Au-Dox leads primarily to non-apoptotic cell death,[27] and is thus able to overcome this resistance. In Dox-sensitive cells, such as cardiomyocytes, this non-apoptotic mechanism is somewhat less effective than the apoptosis caused by free Dox, probably because the bound Au-Dox does not enter the nucleus. Thus Au-Dox is only expected to be more effective than free Dox in cells that are resistant to apoptosis.

Conclusions

Dox alone in B16 cells fits to a model of slow drug buildup, whereas Au-Dox fits to a pattern of initial high drug efficacy followed by a decrease. In cardiomyocytes, the best fit is to a model of increasing drug concentration which then begins to decrease. Cardiomyocytes are less sensitive to Au-Dox than to Dox alone, the opposite of what is seen in B16 cells. FLIM imaging reveals a striking difference between the two cell types: while Au-Dox enters the nuclei of B16 cells, only free Dox enters cardiomyocyte nuclei. The pattern of uptake in the cardiomyocytes is almost entirely endosomal. These results suggest that conjugated Au-Dox is a useful agent for overcoming Dox resistance of apoptosis-resistant cancer cells, and that it might reduce toxicity to non-target organs, particularly the heart.

In addition, the real-time imaging technique is of general utility and provides a rapid, less labor-intensive approach to development of quantitative drug uptake and cell-killing models.

Acknowledgements

Notes and references

1 P. Vejpongsa and E. T. H. Yeh, *J. Am. Coll. Cardiol.*, 2014, **64**, 938–945.

2 M. Bhave, A. N. Shah, N. Akhter and S. T. Rosen, *Curr. Opin. Oncol.*, 2014, **26**, 590–599.

3 I. Marques-Aleixo, E. Santos-Alves, D. Mariani, D. Rizo-Roca, A. I. Padrao, S. Rocha-Rodrigues, G. Viscor, J. R. Torrella, R. Ferreira, P. J. Oliveira, J. Magalhaes and A. Ascensao, *Mitochondrion*, 2015, **20**, 22–33.

4 J. Czepas and K. Gwozdzinski, *Biomed. Pharmacother.*, 2014, **68**, 1149–1159.

5 G. Khan, S. E. Haque, T. Anwer, M. N. Ahsan, M. M. Safhi and M. F. Alam, *Acta Pol. Pharm.*, 2014, **71**, 861–868.

6 C. Henninger, S. Huelsenbeck, P. Wenzel, M. Brand, J. Huelsenbeck, A. Schad and G. Fritz, *Pharmacol. Res.*, 2015, **91**, 47–56.

7 S. Deng, T. Yan, C. Jendrny, A. Nemecek, M. Vincetic, U. Goedtel-Armbrust and L. Wojnowski, *BMC Cancer*, 2014, 14.

8 S. Rivankar, *J. Cancer Res. Ther.*, 2014, **10**, 853–858.

9 E. Tahover, Y. P. Patil and A. A. Gabizon, *Anti-Cancer Drugs*, 2015, **26**, 241–258.

10 M. E. R. O'Brien, N. Wigler, M. Inbar, R. Rosso, E. Grischke, A. Santoro, R. Catane, D. G. Kieback, P. Tomczak, S. P. Ackland, F. Orlandi, L. Mellars, L. Alland, C. Tendler and C. B. C. S. Grp, *Ann. Oncol.*, 2004, **15**, 440–449.

11 R. De Sanctis, A. Bertuzzi, U. Basso, A. Comandone, S. Marchetti, A. Marrari, P. Colombo, R. F. Lutman, L. Giordano and A. Santoro, *Anticancer Res.*, 2015, **35**, 543–547.

12 M.-Y. Lien, L.-C. Liu, H.-C. Wang, M.-H. Yeh, C.-J. Chen, S.-P. Yeh, L.-Y. Bai, Y.-M. Liao, C.-Y. Lin, C.-Y. Hsieh, C.-C. Lin, L.-Y. Li, P.-H. Lin and C.-F. Chiu, *Anticancer Res.*, 2014, **34**, 7319–7326.

13 G. Minotti, P. Menna, E. Salvatorelli, G. Cairo and L. Gianni, *Pharmacol. Rev.*, 2004, **56**, 185–229.

14 K. Barabas, J. A. Sizensky and W. P. Faulk, *J. Biol. Chem.*, 1992, **267**, 9437–9442.

15 M. Szwed, A. Laroche-Clary, J. Robert and Z. Jozwiak, *Chem.-Biol. Interact.*, 2014, **220C**, 140–148.

16 D. Lubgan, Z. Jozwiak, G. G. Grabenbauer and L. V. Distel, *Cell. Mol. Biol. Lett.*, 2009, **14**, 113–127.

17 X. Zhang, H. Chibli, R. Mielke and J. Nadeau, *Bioconjugate Chem.*, 2011, **22**, 235–243.

18 R. E. Eliaz, S. Nir, C. Marty and F. C. Szoka, *Cancer Res.*, 2004, **64**, 711–718.

19 J. Pascal, C. E. Ashley, Z. Wang, T. A. Brocato, J. D. Butner, E. C. Carnes, E. J. Koay, C. J. Brinker and V. Cristini, *ACS Nano*, 2013, **7**, 11174–11182.

20 J. W. Zhang, F. Zhou, X. L. Wu, X. X. Zhang, Y. C. Chen, B. S. Zha, F. Niu, M. Lu, G. Hao, Y. Sun, J. G. Sun, Y. Peng and G. J. Wang, *Br. J. Pharmacol.*, 2012, **165**, 120–134.

21 J. S. Basuki, H. T. T. Duong, A. Macmillan, R. B. Erlich, L. Esser, M. C. Akerfeldt, R. M. Whan, M. Kavallaris, C. Boyer and T. P. Davis, *ACS Nano*, 2013, **7**, 10175–10189.

22 G. Romero, Y. Qiu, R. A. Murray and S. E. Moya, *Macromol. Biosci.*, 2013, **13**, 234–241.

23 Y. Li, H. T. Duong, S. Laurent, A. MacMillan, R. M. Whan, L. V. Elst, R. N. Muller, J. Hu, A. Lowe, C. Boyer and T. P. Davis, *Adv. Healthcare Mater.*, 2015, **4**, 148–156.

24 T. T. N'Guyen, H. T. Duong, J. Basuki, V. Montembault, S. Pascual, C. Guibert, J. Fresnais, C. Boyer, M. R. Whittaker, T. P. Davis and L. Fontaine, *Angew. Chem., Int. Ed.*, 2013, **52**, 14152–14156.

25 X. Zhang, S. Shastry, S. E. Bradforth and J. L. Nadeau, *Nanoscale*, 2015, **7**, 240–251.

26 J. M. de la Fuente, C. C. Berry, M. O. Riehle and A. S. Curtis, *Langmuir*, 2006, **22**, 3286–3293.

27 X. Zhang, J. G. Teodoro and J. L. Nadeau, *Nanomedicine*, 2015, 1365–1375.

28 A. Yerlikaya and N. Erin, *Int. J. Mol. Med.*, 2008, **22**, 817–823.

29 H. Kosano, T. Kayanuma and H. Nishigori, *Biochim. Biophys. Acta, Mol. Cell Res.*, 2000, **1499**, 11–18.

30 J. Trögl and K. Benediktová, *Int. J. Environ. Res*, 2011, **5**, 989–998.

31 M. Andraud, C. Chauvin, P. Sanders and M. Laurentie, *Antimicrob. Agents Chemother.*, 2011, **55**, 756–761.

32 S. N. Gardner, *Cancer Res.*, 2000, **60**, 1417–1425.

33 P. Vichi and T. R. Tritton, *Cancer Res..*, 1989, **49**, 2679–2682.

34 S. N. Gardner, *Cancer Res.*, 2000, **60**, 1417–1425.

35 M. J. H. Janssen, D. J. A. Crommelin, G. Storm and A. Hulshoff, *Int. J. Pharm.*, 1985, **23**, 1–11.

36 X. Zhang, S. Shastry, S. E. Bradforth and J. L. Nadeau, *Nanoscale*, 2015, **7**, 240–251.

37 M. Bontenbal, A. M. Sieuwerts, H. A. Peters, P. Sonneveld, J. A. Foekens and J. G. Klijn, *J. Steroid Biochem. Mol. Biol.*, 1990, **37**, 1097–1101.

38 P. Ma and R. J. Mumper, *Nano Today*, 2013, **8**, 313–331.

39 F. Wang, Y. C. Wang, S. Dou, M. H. Xiong, T. M. Sun and J. Wang, *ACS Nano*, 2011, **5**, 3679–3692.

40 P. Chaudhuri, S. Soni and S. Sengupta, *Nanotechnology*, 2010, **21**, 025102.

41 Y. Fan, C. Li, H. Cao, F. Li and D. Chen, *Biomaterials*, 2012, **33**, 4220–4228.

42 Y. A. Hannun, *Blood*, 1997, **89**, 1845–1853.